On the Room-Temperature Mechanical Properties of an Ion-Irradiated TiZrNbHfTa Refractory High Entropy Alloy

MICHAEL MOSCHETTI,[1] ALAN XU,[2,3] BENJAMIN SCHUH,[4]
ANTON HOHENWARTER,[5] JEAN-PHILIPPE COUZINIÉ,[6]
JAMIE J. KRUZIC,[1] DHRITI BHATTACHARYYA,[2,3]
and BERND GLUDOVATZ [1,7]

1.—School of Mechanical and Manufacturing Engineering, UNSW Sydney, Sydney, NSW 2052,
Australia. 2.—School of Materials Science and Engineering, UNSW Sydney, Sydney, NSW 2052,
Australia. 3.—Australian Nuclear Science and Technology Organisation (ANSTO), Lucas Heights,
NSW 2234, Australia. 4.—Erich-Schmid-Institute of Materials Science, Austrian Academy of
Sciences, 8700 Leoben, Austria. 5.—Department of Materials Science, Chair of Materials Physics,
Montanuniversität Leoben, 8700 Leoben, Austria. 6.—Université Paris Est, ICMPE (UMR 7182),
CNRS, UPEC, 94320 Thiais, France. 7.—e-mail: b.gludovatz@unsw.edu.au

Refractory high-entropy alloys (RHEAs) are potential candidate materials for use in next-generation nuclear reactors due to their excellent mechanical performance at high temperatures. Here, we investigate the microstructure and mechanical properties of the nanocrystalline RHEA TiZrNbHfTa before and after irradiation with He^{2+} ions to determine radiation-induced property changes. Using nanoindentation and in situ microtensile testing we find only small changes in hardness after irradiation but a significant increase in yield and ultimate tensile strength without loss in ductility. This is associated with radiation hardening and a shift from shear localization failure with smooth fracture surfaces to a fracture morphology consisting of fine dimples and intergranular failure characteristics. Overall, the material shows excellent damage-tolerant properties with good combinations of strength and ductility both prior to and after ion irradiation.

INTRODUCTION

The next generation of nuclear reactors is designed to utilize fuel more efficiently to yield significantly higher amounts of energy while producing lower quantities of radioactive waste thereby meeting global challenges such as the ever-increasing energy demand and environmental pollution. These Generation-IV reactors will operate under extremely demanding environments, the core components being subjected to significantly higher levels of radiation and increased operational temperatures compared with previous generations.[1] A principal barrier in their development is the lack of structural materials that have the required radiation-damage tolerance for long-term reactor operation.[1–3]

High-entropy alloys (HEAs)—also commonly referred to as compositionally complex alloys (CCAs) or multi-principal-element alloys (MPEAs)—represent a relatively new family of alloys that exist within the vastly unexplored central area of alloy-compositional space. These alloys comprise several principal elements and have shown exceptional mechanical properties, unique phase stabilization capability, and high tolerance for radiation, indicating potential for use as structural materials in next-generation nuclear applications.[4–10]

Refractory high-entropy alloys (RHEAs) are a subgroup that are most often single-phase body-centered cubic (BCC) HEAs, and some of them show exceptional mechanical properties at high temperature.[6,11] They have the potential to be disruptive to the high-temperature structural materials market—a market typically dominated by superalloys—and may be suitable candidate materials for the requirements of next-generation nuclear reactors. TiZrNbHfTa, one of the most studied RHEAs to date, has excellent mechanical properties over a large temperature range and exhibits significant

(Published online November 4, 2019)

ductility that allows for extensive deformation (e.g., through cold-rolling) which is uncommon amongst BCC-structured HEAs.[12–14] After processing to obtain recrystallized grains with sizes from ~50 μm to 200 μm, the material comprises a single-phase BCC structure at room temperature, has a tensile ductility of approximately 10%, and has a yield strength of ~ 800 MPa in tension.[12,14] However, the single-phase structure at room temperature is thermodynamically unstable, and the formation of additional hexagonal closed-packed (HCP) and BCC phases has been observed at temperatures as low as 500°C.[14,15] Nevertheless, as the effect of irradiation on RHEAs has rarely been studied[16,17] and TiZrNbHfTa is one of few BCC-structured HEAs with appreciable ductility, it presents a suitable material for investigation of the effects of ion irradiation on RHEAs; the effect of irradiation on the microstructure and mechanical properties of TiZrNbHfTa has, to the knowledge of the authors, not been reported on before.

In this work, we have subjected the material to high-pressure torsion (HPT) and subsequent irradiation by He^{2+} ions to a damage dose of ~ 1 dpa (displacement per atom), with the aim of assessing its post-irradiation mechanical performance and radiation damage tolerance. The material was HPT-deformed to induce a nanocrystalline grain structure prior to the irradiation treatment and was subsequently characterized by nanoindentation and microtensile testing. The small grain size ensures that a significant number of grains are irradiated through the depth of the sample and that the microtensile samples can include a large number of grains so as to provide mechanical properties comparable to those obtained through conventional testing.

METHODS

Material Synthesis

The equiatomic TiZrNbHfTa RHEA was prepared by arc-melting raw materials exceeding 99.9% purity under Ar atmosphere on a water-cooled copper plate, homogenized by high-frequency induction heating in a cooled copper crucible, and finally arc-melted once more prior to casting into an ingot of approximately 60 mm length and 10 mm diameter. Details of the preparation procedure can be found elsewhere.[13] The material was then cold-rolled to 0.8 mm thickness (~ 80% reduction), recrystallized at 1100°C for 5 h, and 'air-cooled' in He atmosphere. Material in this state is referred to as recrystallized material throughout the text. Elemental composition of the recrystallized material was determined by inductively coupled plasma atomic emission spectroscopy (ICP-AES). Discs of 8 mm diameter were cut by electrical discharge machining (EDM) and severely plastically deformed using HPT with the same parameters as described in Ref. 14. Material in this state is referred to as

HPT material throughout the text. The HPT discs were sliced into eight equal pieces. Their surfaces were ground and polished using SiC paper up to 4000 grit followed by a final polishing step using a 0.04-μm colloidal silica suspension on a TegraPol-11 (Struers, USA).

Ion Irradiation

Specimens were irradiated at room temperature with He^{2+} ions at an energy of 5 MeV and a flux of 1.6×10^{12} ions/(cm² s) to a fluence of 4.4×10^{17} ions/cm² in the 2 MV STAR Tandem Accelerator at the Centre for Accelerator Science of Australia's Nuclear Science and Technology Organisation (ANSTO, Australia). The sample temperature during irradiation was not measured, however, in previous experiments with similar treatments the sample temperature did not exceed ~50 °C, which is considered negligible for this RHEA. The energy was attenuated by a degrader wheel, which functions by rotating a disc consisting of 20 radially segmented aluminum foils of different thickness that intersect the ion beam and reduce the incident ion energy by an amount proportional to the respective foil thickness, consequently spreading the ion energies and hence penetration depth over a larger range.

The profile of the radiation-induced damage and concentration of implanted He in the target material was simulated using the SRIM (Stopping and Range of Ions in Matter-2013) software package.[18] The energy spectrum post-degrader wheel was determined by the 'stopping/range tables' of He into Al, and the damage profile and He concentration
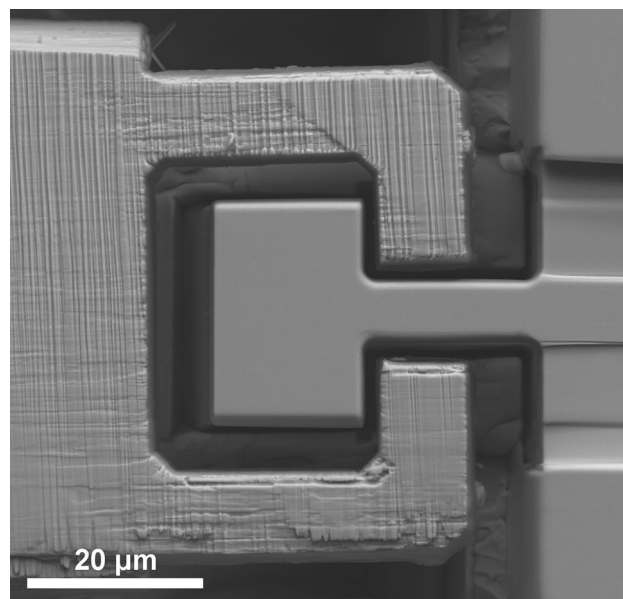

Fig. 1. In situ microtensile tests were performed in an SEM for both unirradiated and irradiated samples with a cross section of ~ 5 μm × 5 μm and a gauge length of ~ 16 μm.

were determined by the TRIM (TRansport of Ions in Matter) package included in SRIM, where the target layer was equiatomic TiZrNbHfTa with a density of $\rho = 9.94$ g/cm^3.[12] Displacement energies were obtained from the literature with Ti = 30 eV, Zr = 40 eV, Nb = 78 eV, Hf = 61 eV, and Ta = 91 eV.[19] Simulations were performed for a total of 10^5 incident ions using the "detailed calculation with full damage cascades" model.

Microstructural Characterization

The microstructure of the recrystallized material before the HPT deformation was characterized in an UltraPlus^{TM} (Zeiss$^®$, Germany) scanning electron microscope (SEM). Grain size, texture, and crystal structure were determined using electron backscatter diffraction (EBSD). To characterize the microstructure of the HPT samples, TEM foils were produced by focused-ion-beam (FIB) milling using Ga$^+$ ions in an Auriga 60 Cross-beam^{TM} instrument (Zeiss$^®$, Germany). Grain size, crystal structure, and lattice parameters were determined by bright-field transmission electron microscopy (BF-TEM) and selected area diffraction (SAD) on a 2200FS^{TM} TEM (JEOL$^®$, Japan). SAD patterns were measured and manually indexed to the reflecting planes of the expected crystal lattices.[20]

Table I. Elemental composition (in at.%)

Element	Concentration
Ti	20.67
Zr	19.51
Nb	19.28
Hf	19.67
Ta	20.78

Micromechanical Properties

Nanoindentation was performed with a Nano Indenter G300 (Agilent$^®$, USA) in continuous stiffness measurement (CSM) mode using a diamond Berkovich tip. At least 14 indents were made per specimen to a depth of 2 μm and spaced 100 μm apart, with an oscillatory tip displacement of 4 nm at 45 Hz. Hardness versus indentation depth profiles were recorded directly by the system.

Dog-bone-shaped microtensile specimens with a cross-section of approximately 5 μm × 5 μm and a gauge length of 16 μm (Fig. 1) were FIB-milled from both the unirradiated and ion-irradiated HPT samples. Microtensile tests were conducted in situ using an MTR-3^{TM} (MicroTesting Solutions$^®$, USA) microtensile testing rig mounted inside the SEM. The samples were pulled using the custom tensile grips shown in Fig. 1 at a displacement rate of ~ 0.3 nm/s; the tests were paused intermittently at predetermined displacement intervals to capture SEM images and calculate strain at the gauge shoulders using digital image correlation (DIC) with a custom MATLAB code. In total, six samples were tested, three per condition; one of the irradiated samples failed outside the gauge section and was hence excluded from the results. Post-failure images of the fracture surfaces were taken in an Ultra-Plus^{TM} SEM (Zeiss$^®$, Germany).

RESULTS

Microstructure

ICP-AES analysis of the TiZrNbHfTa alloy revealed a near-equiatomic elemental composition with somewhat higher amounts of Ti and Ta, and correspondingly lower Zr, Nb, and Hf concentrations, as shown in Table I. EBSD scans of the recrystallized material show equiaxed grains of ~ 80 μm diameter with a slight texture remaining from the rolling process (Fig. 2a), similar to Ref. 21.

BF-TEM of both unirradiated (Fig. 2b) and irradiated (Fig. 2c) HPT samples show a grain size of
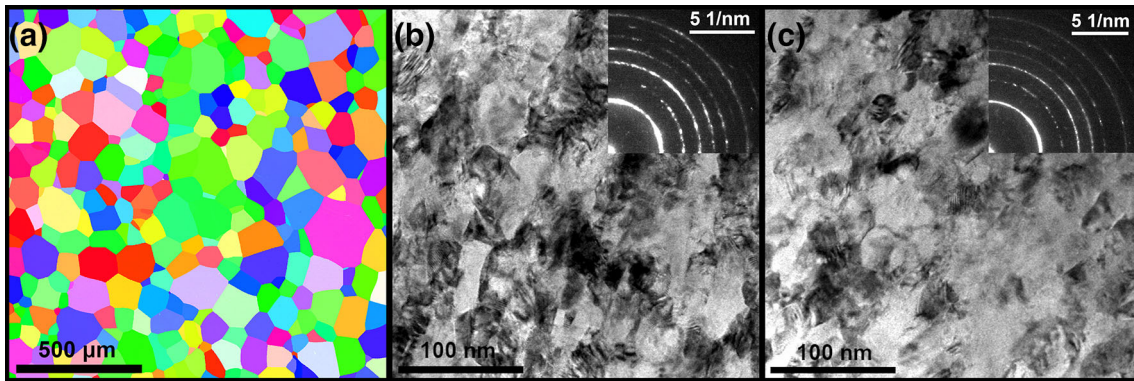
Fig. 2. TiZrNbHfTa microstructure of (a) the recrystallized material; the EBSD map shows equiaxed grains of ~ 80 μm. TEM images of (b) unirradiated and (c) irradiated HPT-deformed material reveal a grain size of ~ 40 nm.
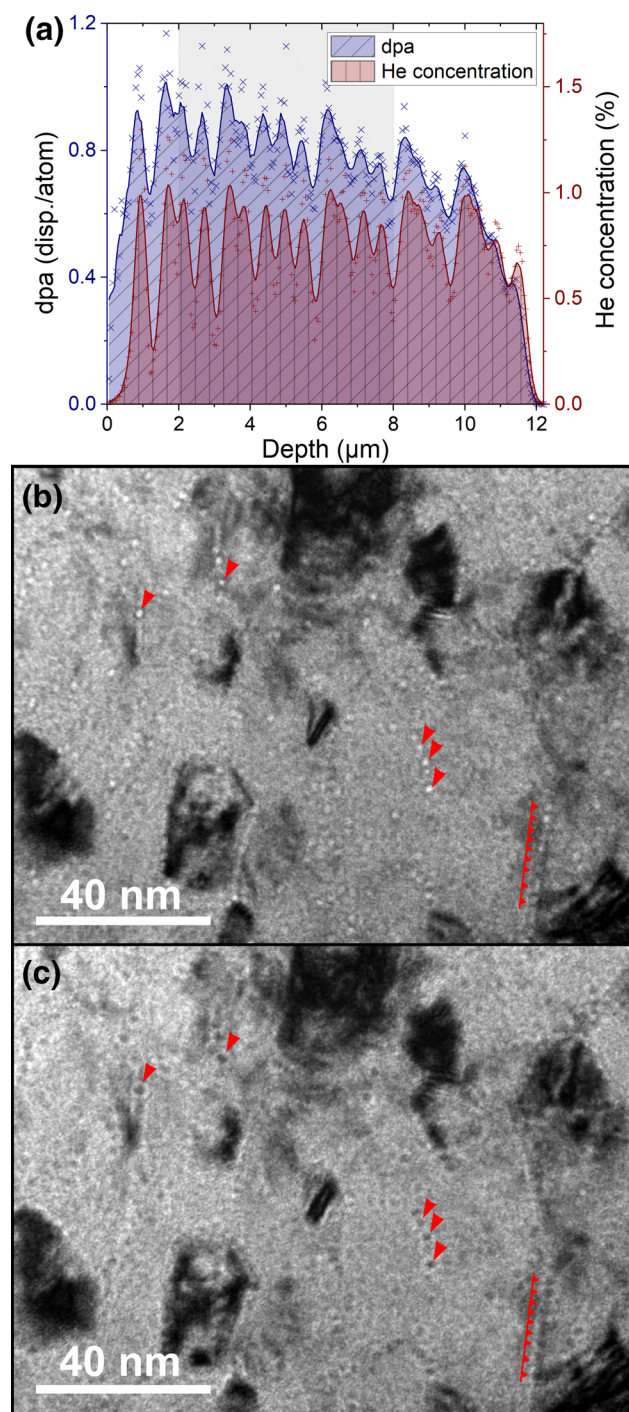
Fig. 3. Radiation-induced damage represented by (a) the SRIM damage profile and induced He concentration over irradiation depth, showing a relatively uniform region between 2 μm and 8 μm. Both raw data and 5-point moving average fits are shown; (b and c) are TEM images taken 2 μm under- and over-focused, respectively, showing Fresnel fringes indicative of He bubbles (bright or dark spots in under- or over-focus conditions, respectively). Red arrows highlight particularly notable bubbles, many of which are located at grain interfaces.
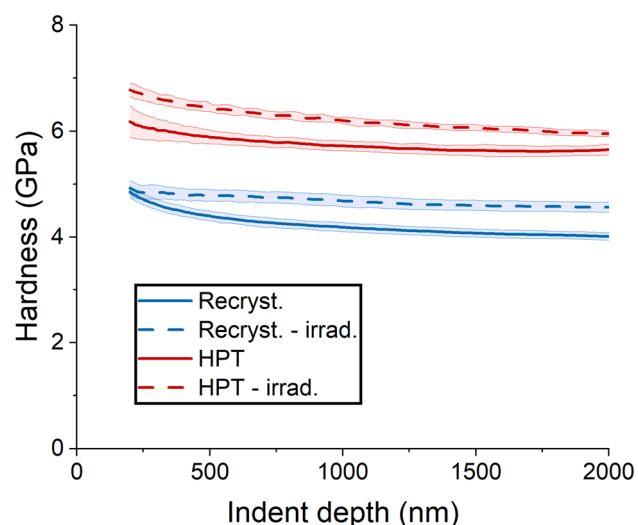

Fig. 4. Nanoindentation results of the recrystallized and HPT samples of both irradiated and unirradiated conditions showing hardness over indent depth. Shaded areas around lines show a standard deviation of at least 14 indentations.
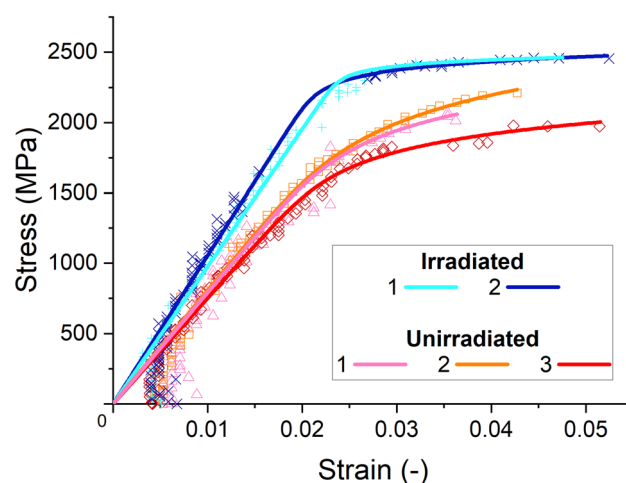

Fig. 5. Tensile stress–strain curves of both irradiated and unirradiated HPT specimens, where engineering stress and strain were determined in situ inside of an SEM. Both individual data points and a Ramberg–Osgood fit are shown. Each data set is aligned such that the Ramberg-Osgood fit intersects the origin.

$\sim$ 40 nm, similar to Refs. [14] and [22], with Moiré fringes in both cases obvious across several grains. SAD patterns of the unirradiated HPT sample

(Fig. [2]b inset) are consistent with a BCC structure, and the calculated lattice parameter of $a = 3.35$ Å is in close agreement with published data.[12–14,22–25] The lattice parameter in samples after irradiation was essentially identical at $a = 3.36$ Å (Fig. [2]c inset).

Radiation Damage Profile

The SRIM-determined damage profile (Fig. [3]a) decreases only slightly with depth and has an average radiation-induced damage of $\sim$ 0.8 dpa for a penetration depth of $\sim$ 2–10 μm, followed by a sharp decay up to $\sim$ 12 μm. Fresnel fringes indicative of agglomerated He in the form of bubbles[26,27]

Table II. Key tensile properties of the HPT-processed material

	Yield strength (MPa)	Ultimate strength (MPa)	Elastic modulus (GPa)	Failure strain (%)
Unirradiated				
1	1913	2129	78.6	5.15
2	1766	2211	79.9	3.63
3	1821	1979	77.0	4.28
Average ($\pm$ SD)	1833 $\pm$ 61	2106 $\pm$ 96	78.5 $\pm$ 1.4	4.35 $\pm$ 0.62
Irradiated				
1	2084	2490	101.3	4.09
2	2092	2459	108.1	5.25
Average ($\pm$ SD)	2088 $\pm$ 4	2475 $\pm$ 16	104.7 $\pm$ 3.4	4.67 $\pm$ 0.58
Radiation-induced increase	13.9%	17.5%	33.4%	7.4%

were observed across the $\sim$ 10-μm-wide TEM foil of the irradiated HPT samples (Fig. 3b, c), preferentially located on grain boundaries. However, there was very little evidence of so-called "black dot damage" typically found in ion-irradiated metallic materials.

Micromechanical Properties

Nanoindentation

Hardness profiles from nanoindentation of both recrystallized and HPT-deformed samples, before and after irradiation, are shown in Fig. 4. The first 200 nm of each test series was considered unreliable because of contact issues and indentation size effect (ISE)[28] at very low depths and thus was excluded from the plots.

Prior to irradiation, the HPT-deformed material shows more than a $\sim$ 35% increase in hardness (i.e., 4.2 GPa to 5.7 GPa) relative to the recrystallized material across depths of 800–1200 nm (Fig. 4). This depth range represents the region where the influence of ISE and of the unirradiated subsurface of the material are expected to be minimized.* Irradiation of both the recrystallized and HPT-deformed samples results in a $\sim$ 10% higher hardness compared with the unirradiated states (4.2-4.6 GPa and 5.7-6.2 GPa over 800–1200 nm depths, respectively). These nanohardness values using a Berkovich tip and a maximum load < 200 mN are notably higher than previously reported microhardness data determined using Vickers hardness with a load of 1 kg ($\sim$ 10 N).[14] Irradiation of the recrystallized material results in a flatter hardness profile which indicates a reduction in the magnitude of ISE. Previous work on single-crystal Mo found a similar result, attributing it to a reduction in pop-in load caused by radiation-induced defects[30], however, a similar reduction is not seen in the HPT-processed material.

Microtensile Testing

Engineering stress–strain curves of three unirradiated and two irradiated HPT samples are shown in Fig. 5, along with their respective fits to the Ramberg–Osgood equation:

$$\varepsilon = \frac{\sigma}{E} + \left(\frac{\sigma}{K}\right)^n, \tag{1}$$

where E is the Young's modulus, and K and n are material-dependent constants. Compared with the unirradiated samples, the irradiated samples exhibit a roughly 14% increase in average yield strength values from 1833 MPa to 2088 MPa and stiffness values from $\sim$ 79 GPa to $\sim$ 105 GPa, and an increase in ultimate tensile strength from 2106 MPa to 2475 MPa, with no apparent decrease in strain to failure, which remained essentially unchanged at around 4.5% strain; the individual values of each tested sample are listed together with averaged numbers in Table II.** The results compare well to previously reported values from macroscopic tensile tests on unirradiated, HPT-processed TiZrNbHfTa with the exception of elongation to failure, which sees a reduction of approximately 45% when compared with equivalently processed material.[14]

SEM images taken from the fracture surfaces of the samples after testing showed two distinct fracture patterns; the unirradiated samples (Fig. 6a) fracture approximately 45° from the loading direction (Fig. 6a inset) and exhibit a relatively smooth fracture surface with several pronounced ridges separating the smooth areas, whereas the irradiated samples (Fig. 6b) exhibit a notably rougher fracture surface that failed essentially perpendicular to the loading direction (Fig. 6b inset). These fracture surfaces exhibit an obvious grain structure, and both micro-dimples and regions of grain pullout associated with the remaining ductility after the

---

*The indenter-induced plastic zone is estimated using $R_{\text{plastic}}/d_{\text{indent}} = 8$, where R_{plastic} is the plastic zone radius and d_{indent} is the indent depth.[29]

**It should be noted that our reported failure strains have been extracted from the DIC measurements of images taken intermittently and hence slightly underestimate the actual failure strain.
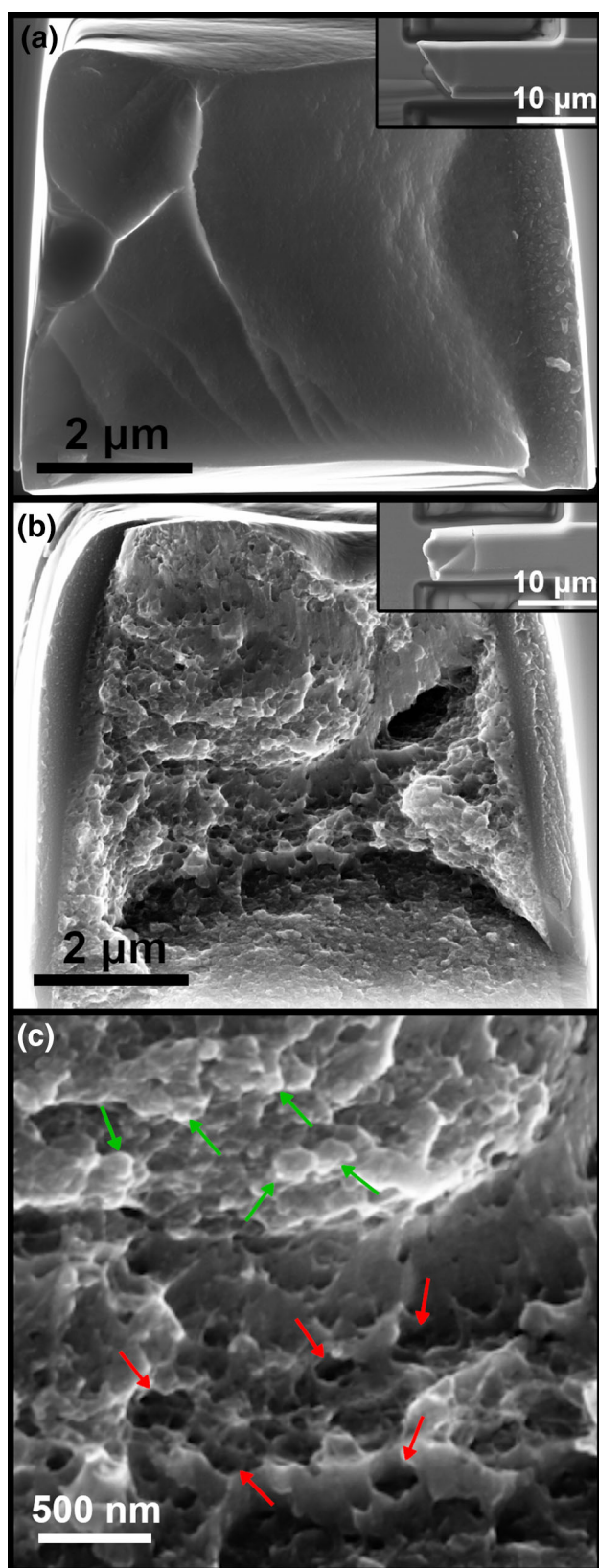
◄Fig. 6. Fracture surface images of the (a) unirradiated and (b) irradiated HPT specimens with respective top-down views inset. The unirradiated specimens fractured 45° from the loading direction and show a predominantly smooth surface with some ridges, while the irradiated material exhibits an obvious grain structure (green arrows) and regions of both micro-dimples and grain pullout (red arrows), as shown in (c), which is a magnified section of (b).

irradiation treatment, all highlighted in Fig. 6c. Additionally, the irradiated samples show larger-sized elongated void formation and shear lips at the sample edges. Specimens from both conditions showed limited necking. Cross sections exhibit a somewhat trapezoidal geometry due to defocusing of the FIB beam and a thin redeposition layer from the milling process. The redeposited material peeled off in some cases during testing and does not contribute significantly to the overall mechanical properties as it is loosely deposited on the sample surface; we have therefore measured the angles of the trapezoidal cross section of our samples after testing, excluded the thickness of the redeposited material, and used these values for the calculation of the original cross-sectional area and subsequently the stress–strain curves.

DISCUSSION

TEM analysis of the HPT samples after irradiation with He^{2+} ions did not show any change in grain size or morphology (Fig. 2c) to account for the observed hardness differences (Fig. 4). However, Fresnel fringes (Fig. 3b, c) indicative of He bubbles clearly revealed radiation-induced damage occurred in the material. Helium is known to preferentially segregate to grain boundaries.[30] For example, previous works on He ion-irradiated austenitic stainless steel and TiAl alloy reported defect-free zones up to ∼ 30–50 nm adjacent to the grain boundaries indicating that such boundaries act as sinks for He atoms and defects.[26,30] While nanoindentation of the recrystallized material generally occurs within a single grain, the HPT material has significantly smaller grains, resulting in the inclusion of many grain boundaries in each indent. Therefore, hardening of the recrystallized material is attributed to lattice defects typical of radiation-induced hardening (e.g., vacancy clusters, dislocation loops, etc.), while hardening of the HPT material is attributed to a combination of He at the grain boundaries in addition to such lattice defects. The fact that a reduction in magnitude of ISE is seen in the irradiated, recrystallized material and not the HPT-processed material supports that the grain boundaries in the HPT-processed material likely act as sinks for such defects. As shown in Table III, the ∼ 10% increase in hardness for both recrystallized and HPT-deformed materials after irradiation is significantly less than typically seen for austenitic stainless steels (SS316/SS316LN[29,31,32]), titanium

Table III. Radiation-induced hardness of materials reported in the literature

	∆ Hardness (% (GPa))	Irradiation treatment					Grain size (µm)
		Damage (dpa)	Energy (MeV)	Ion species (–)	Temperature (°C)	Reference depth (nm)	
TiZrNbHfTa (this study)							
Recrystallized	8%	0.8	5 (w/degrader)	He^{2+}	rt	800–1200	80
HPT	10%						0.04
SS316[a29]	54% (2.7 to 4.1)	6.7 (peak)	1	He^{2+}	rt	400	50–70
SS316[ab31]	52% (3.3 to 5)	8.6 (peak)	0.2, 0.4	He$^+$, He^{2+}	rt	200	–
SS316LN[ab32]	41%	1 (peak)	.36	He	200	150	–
45XD TiAl[33]	54% (5.6 to 8.5)	1	5 (w/degrader)	He^{2+}	rt	300–400	–
Ti-6Al-4V[ab31]	38% (4.3 to 5.8)	6.6 (peak)	0.2, 0.4	He$^+$, He^{2+}	rt	200	–
MA956 ODS[a34]	25% (6 to 7.5)	0.46	0.015 to 0.5	He	rt	180	–
MA957 ODS[ab31]	40% (5 to 7)	8.6 (peak)	0.2, 0.4	He$^+$, He^{2+}	rt	200	–
PM2000[a] (ODS)[35]		1.4 (1–2 µm)	1.5 (4 incidence)	He^{2+}	rt	500	
Annealed	15%						Coarse
SPD	16%						fine
Zircaloy-4[ab31]	38% (2.5 to 2.4)	7.9 (peak)	0.2, 0.4	He$^+$, He^{2+}	rt	200	–
nc Ni[a36]	31% (2.9 to 3.8)	0.1	12 (w/degrader)	He^{2+}	rt	~180	Nanocrystalline

[a]Damage is reported as a peak value and not a depth-averaged value. The depth-averaged value that is measured by nanoindentation would be notably lower. [b]Values interpreted visually from figure

alloys (45XD TiAl, Ti-6Al-4Vab,[31,33]), oxide dispersion-strengthened (ODS) steels (MA956/957, PM2000[31,34,35]), and other alloys[31,36] subjected to similar irradiation treatments. This observation is in agreement with the fact that the number of "black dot damage" features visible in the interiors of the grains is relatively small.

Although radiation-induced hardening is typically accompanied by a loss in ductility, the microtensile results for the HPT samples revealed no loss in ductility, or perhaps even a slight increase, after irradiation, as shown in Fig. 5 and Table II. This can be explained by the observed differences in the deformation and failure mechanisms seen in Fig. 6. Nanocrystalline metals are prone to a saturation of strain hardening at relatively low strains that results in failure by shear localization (i.e., shear banding, as seen in Fig. 6-a).[37] This process is thought to involve dislocation generation and annihilation at grain boundaries without being significantly impeded in their mobility.[37] Shear localization is further promoted by the small sample cross section that induces a condition of plane stress across the sample cross section. Accordingly, the tri-axial stresses necessary for the classical microvoid coalescence failure mechanism observed by Schuh et al.[14] for macroscopic tensile tests of unirradiated HPT material are not possible. The shear localization observed for the microtensile samples in the present study (Fig. 6a) is responsible for the somewhat smaller failure strain ($\sim$ 4.7%) compared with the macroscopic tests in Ref. 14 ($\sim$ 8% strain). In contrast, the failure mechanism for the irradiated samples is distinctly different (Fig. 6b).

In ultra-fine-grained and nanocrystalline metals, it has been observed that the strength and ductility can be increased simultaneously by activating grain boundary sliding (GBS) as a deformation mechanism.[38–42] Although GBS is more often thought of as an elevated temperature deformation mechanism requiring temperatures $\geq 0.5\ T_{\mathrm{m}}$, where T_{m} is the melting temperature, it can be induced at much lower temperatures in nanocrystalline materials by reducing the grain size and introducing a large volume of high-energy, high-angle grain boundaries.[38] In the present work, the grain size of the irradiated samples is identical to that of the unirradiated samples; however, He is shown to segregate to the grain boundaries, which will affect their local atomic structure. Accordingly, the higher flow stress levels experienced by the irradiated samples due to radiation hardening in combination with the He-affected grain boundaries are likely to have induced GBS as a competing deformation mechanism. Evidence for this is seen on the fracture surfaces, which show intergranular void formation leaving dimples on the fracture surface, along with intergranular fracture (Fig. 6b, c). The observation of dimples from intergranular void formation is similar to that observed in Ref. 42 for samples

where GBS is thought to be the active deformation mechanism. In the present samples, there appears to be some competition between deformation mechanisms, with shear banding also evident in the irradiated samples (Fig. 6b inset). Enhanced ductility by GBS is often accompanied by higher strain rate sensitivity;[38] accordingly, future work should examine the role of strain rate on the ductility of the irradiated samples to further elucidate the deformation and failure mechanisms. However, overall the present results demonstrate the excellent potential of this alloy to maintain desirable combinations of strength and ductility even after significant irradiation doses.

CONCLUSION

The effect of He^{2+} ion irradiation on the microstructure and mechanical properties of the RHEA, TiZrNbHfTa, with both coarse-grained and nanocrystalline microstructures, was investigated using electron microscopy, nanoindentation, and microtensile testing.

- Both recrystallized and nanocrystalline materials show only a moderate increase in hardness after irradiation, which is attributed to classic radiation hardening due to defect formation in the lattice.
- The tensile stress–strain behavior of the HPT material after irradiation shows a significant increase in both yield and ultimate tensile strength and an increase in stiffness; however, its ductility remains unchanged at $\sim$ 4.5% failure strains.
- The failure mechanism of the unirradiated HPT material is dominated by shear localization at 45° to the loading direction, which is attributed to the nanocrystalline structure and the state of plane stress.
- In the irradiated state, failure occurs perpendicular to the tensile direction and is governed by the formation of nano-sized intergranular voids and intergranular fracture. This is attributed to He weakening grain boundaries and activating grain boundary sliding as a deformation mechanism, which enables higher strength without loss of ductility.

Overall, the material was found to have excellent damage tolerance before and after irradiation compared with typical structural materials targeted for Generation-IV nuclear reactor applications.

CONFLICT OF INTEREST

The authors declare that they have no conflict of interest.

REFERENCES

1. K.L. Murty and I. Charit, *J. Nucl. Mater.* 383, 189 (2008).
2. S.J. Zinkle and J.T. Busby, *Mater. Today* 12, 12 (2009).
3. L.K. Mansur, A.F. Rowcliffe, R.K. Nanstad, S.J. Zinkle, W.R. Corwin, and R.E. Stoller, *J. Nucl. Mater.* 329–333, 166 (2004).
4. Y. Zhang, T.T. Zuo, Z. Tang, M.C. Gao, K.A. Dahmen, P.K. Liaw, and Z.P. Lu, *Prog. Mater. Sci.* 61, 1 (2014).
5. E.P. George, D. Raabe, and R.O. Ritchie, *Nat. Rev. Mater.* (2019).
6. D.B. Miracle and O.N. Senkov, *Acta Mater.* 122, 448 (2017).
7. F. Granberg, K. Nordlund, M.W. Ullah, K. Jin, C. Lu, H. Bei, L.M. Wang, F. Djurabekova, W.J. Weber, and Y. Zhang, *Phys. Rev. Lett.* 116, 135504 (2016).
8. B. Gludovatz, A. Hohenwarter, D. Catoor, E.H. Chang, E.P. George, and R.O. Ritchie, *Science* 345, 1153 (2014).
9. K.V.S. Thurston, B. Gludovatz, A. Hohenwarter, G. Laplanche, E.P. George, and R.O. Ritchie, *Intermetallics* 88, 65 (2017).
10. K.V.S. Thurston, B. Gludovatz, Q. Yu, G. Laplanche, E.P. George, and R.O. Ritchie, *J. Alloys Compd.* 794, 525 (2019).
11. O.N. Senkov, D.B. Miracle, K.J. Chaput, and J.-P. Couzinié, *J. Mater. Res.* 33, 3092 (2018).
12. O.N. Senkov, J.M. Scott, S.V. Senkova, D.B. Miracle, and C.F. Woodward, *J. Alloys Compd.* 509, 6043 (2011).
13. J.P. Couzinié, G. Dirras, L. Perrière, T. Chauveau, E. Leroy, Y. Champion, and I. Guillot, *Mater. Lett.* 126, 285 (2014).
14. B. Schuh, B. Völker, J. Todt, N. Schell, L. Perrière, J. Li, J.P. Couzinié, and A. Hohenwarter, *Acta Mater.* 142, 201 (2018).
15. O.N. Senkov and S.L. Semiatin, *J. Alloys Compd.* 649, 1110 (2015).
16. Y. Lu, H. Huang, X. Gao, C. Ren, J. Gao, H. Zhang, S. Zheng, Q. Jin, Y. Zhao, C. Lu, T. Wang, and T. Li, *J. Mater. Sci. Technol.* 35, 369 (2019).
17. O. El-Atwani, N. Li, M. Li, A. Devaraj, J.K.S. Baldwin, M.M. Schneider, D. Sobieraj, J.S. Wróbel, D. Nguyen-Manh, S.A. Maloy, and E. Martinez, *Sci. Adv.* 5, eaav2002 (2019).
18. J.F. Ziegler, M.D. Ziegler, and J.P. Biersack, *Nucl. Instrum. Methods Phys. Res. Sect. B Beam Interact. Mater. At.* 268, 1818 (2010).
19. A.Yu. Konobeyev, U. Fischer, Yu.A. Korovin, and S.P. Simakov, *Nucl. Energy Technol.* 3, 169 (2017).
20. R. Abbaschian, L. Abbaschian, and R.E. Reed-Hill, *Physical Metallurgy Principles*, 4th ed. (Stamford, CT: Cengage Learning, 2009).
21. G. Laplanche, P. Gadaud, L. Perrière, I. Guillot, and J.P. Couzinié, *J. Alloys Compd.* 799, 538 (2019).
22. J. Čížek, P. Haušild, M. Cieslar, O. Melikhova, T. Vlasák, M. Janeček, R. Král, P. Harcuba, F. Lukáč, J. Zýka, J. Málek, J. Moon, and H.S. Kim, *J. Alloys Compd.* 768, 924 (2018).
23. N.D. Stepanov, N.Yu. Yurchenko, S.V. Zherebtsov, M.A. Tikhonovsky, and G.A. Salishchev, *Mater. Lett.* 211, 87 (2018).
24. S.Y. Chen, Y. Tong, K.-K. Tseng, J.-W. Yeh, J.D. Poplawsky, J.G. Wen, M.C. Gao, G. Kim, W. Chen, Y. Ren, R. Feng, W.D. Li, and P.K. Liaw, *Scr. Mater.* 158, 50 (2019).
25. J. Zýka, J. Málek, Z. Pala, I. Andršová, and J. Veselý, in *24th International Conference on Metallurgy and Materials* (2015).
26. T. Wei, H. Zhu, M. Ionescu, P. Dayal, J. Davis, D. Carr, R. Harrison, and L. Edwards, *J. Nucl. Mater.* 459, 284 (2015).
27. D. Bhattacharyya, M.J. Demkowicz, Y.-Q. Wang, R.E. Baumer, M. Nastasi, and A. Misra, *Microsc. Microanal.* 18, 152 (2012).
28. W.D. Nix and H. Gao, *J. Mech. Phys. Solids* 46, 411 (1998).
29. M. Saleh, Z. Zaidi, M. Ionescu, C. Hurt, K. Short, J. Daniels, P. Munroe, L. Edwards, and D. Bhattacharyya, *Int. J. Plast.* 86, 151 (2016).
30. P.L. Lane and P.J. Goodhew, *Philos. Mag. A* 48, 965 (1983).
31. P. Dayal, D. Bhattacharyya, W.M. Mook, E.G. Fu, Y.-Q. Wang, D.G. Carr, O. Anderoglu, N.A. Mara, A. Misra, R.P. Harrison, and L. Edwards, *J. Nucl. Mater.* 438, 108 (2013).
32. J.D. Hunn, E.H. Lee, T.S. Byun, and L.K. Mansur, *J. Nucl. Mater.* 282, 131 (2000).
33. T. Wei, A. Xu, H. Zhu, M. Ionescu, and D. Bhattacharyya, *Nucl. Instrum. Methods Phys. Res. Sect. B Beam Interact. Mater. At.* 409, 288 (2017).
34. H. Zhang, C. Zhang, Y. Yang, Y. Meng, J. Jang, and A. Kimura, *J. Nucl. Mater.* 455, 349 (2014).
35. M.A. Pouchon, J.C. Chen, and W. Hoffelner, *Adv. Mater. Res.* 59, 269 (2008).
36. G. Sharma, P. Mukherjee, A. Chatterjee, N. Gayathri, A. Sarkar, and J.K. Chakravartty, *Acta Mater.* 61, 3257 (2013).
37. M.A. Meyers, A. Mishra, and D.J. Benson, *JOM* 58, 41 (2006).
38. P. Kumar, M. Kawasaki, and T.G. Langdon, *J. Mater. Sci.* 51, 7 (2016).
39. R.Z. Valiev, I.V. Alexandrov, Y.T. Zhu, and T.C. Lowe, *J. Mater. Res.* 17, 5 (2002).
40. R. Valiev, *Nat. Mater.* 3, 511 (2004).
41. T. Mungole, P. Kumar, M. Kawasaki, and T.G. Langdon, *J. Mater. Sci.* 50, 3549 (2015).
42. T. Mungole, P. Kumar, M. Kawasaki, and T.G. Langdon, *J. Mater. Res.* 29, 2534 (2014).